Nanoscale morphology, tribology and electrical properties of polyaniline/graphene oxide/Laponite composites investigated using atomic force microscopy

Journal:	*Nanoscale*
Manuscript ID	NR-ART-07-2019-005713.R1
Article Type:	Paper
Date Submitted by the Author:	13-Oct-2019
Complete List of Authors:	Ramphal, Isaac; Union College, Chemistry Hagerman, Michael; Union College, Chemistry

Nanoscale morphology, tribology and electrical properties of polyaniline/graphene oxide/Laponite composites investigated using atomic force microscopy

Isaac Alexander Ramphal and Michael Eugene Hagerman*

Union College Department of Chemistry, 807 Union Street, Schenectady, NY 12308, USA

Abstract

Polyaniline composites with graphene and graphene oxide have received broad interest for applications in charge separation and storage in electrical devices. Syntheses via *in situ* polymerization of aniline in colloidal dispersions of graphene oxide have afforded nanocomposites of polyaniline intercalated within graphene oxide nanosheets. The simultaneous inclusion of Laponite nanoparticles has improved aqueous phase processability and thin film formation. Mechanical, morphological and conductivity studies including atomic force microscopy and scanning electron microscopy were employed to study the host-guest interactions and heterointerfaces that govern self-assembly. Adhesion and conductivity values within graphene oxide/polyaniline/Laponite (GOPL) nanocomposites were tuned by varying the weight ratios of polyaniline:graphene oxide. These studies inform ongoing work to use GOPL nanomaterials for clean energy harvesting and storage applications.

Introduction

Polyaniline and its composites with graphitic materials have received widespread interest in applications as diverse as electrochemical capacitors,[1] photovoltaics,[2] thermoelectrics,[3] chemical sensors,[4] and radionuclide sequestration,[5] among many others. The molecular and nanoscale structure and morphology of these composites have a profound impact on the resulting material properties. The authors defer to Tran et al. for a discussion of how many unique nanostructures of polyaniline depend on variations in select morphosynthetic parameters.[6] Growth of polyaniline separate from, alongside, or grafted to graphitic materials such as graphene, graphene oxide, and carbon nanotubes increases both the range of applications and complexity of the polymeric system. Optimizing synthetic protocols to preferentially yield certain micro- and nanostructures within these composites will facilitate the rational development of new technologies such as those listed above.

The use of colloidal dispersions to alter polymer synthesis conditions and act as templating agents has been widely explored. The synthetic hectorite clay Laponite (RD) has received particular interest for its interesting phase diagram and synthesis templating capabilities.[7-10] Laponite clay particles are 30 nm diameter disks with 1 nm thickness,[11] and have previously been used to study colloidal dispersions of graphene,[12] graphene oxide,[13] and polyaniline.[14] The addition of Laponite to polyaniline/graphene oxide composites was found to promote the formation of fibrous, microporous polyaniline without loss of electroactive response in the composites.[15]

Atomic Force Microscopy (AFM) provides a powerful means to study both the structure as well as the physical properties of materials. Due to the exceptional spatial resolution and high force sensitivity of AFM techniques, material properties can be related very precisely to particular morphological features in the sample. In addition to topographical profiles, operating in dynamic AFM modes produces information on the phase of the cantilever oscillation. Changes in phase have been shown to depend on factors such as viscoelasticity, adhesion forces, and tip-surface contact area.[16] Mechanical and tribological properties of materials can be further characterized by Single Molecule Force Spectroscopy (SMFS) techniques, where local properties such as moduli and tip-sample forces can be measured.[17-18] In conductive AFM (cAFM), a voltage bias applied between the cantilever and sample results in electron conduction into and/or through the sample, achieving localized current-voltage (I-V) characterization of the sample.[18-19]

AFM has been widely applied to study the morphology of polymer composites and their constituent materials. To date, SMFS and cAFM have been employed to provide only very brief commentary of the current-voltage[20] and force-distance[21] curves in polyaniline/graphene and polyaniline/graphene oxide composite systems. Despite the useful information that can be garnered from these types of data, they represent only a single point on the material surface. To construct a broader picture of the electrical and tribological properties of the surface over a given area, conductivity and force maps can be generated. These have been studied for polyaniline and graphene oxide individually,[22-25] as well as limited work done on polyaniline composite materials.[26-27]

This work presents a systematic study of the nanoscale morphological, electrical, and mechanical properties of composites of polyaniline grown in the presence of graphene oxide and Laponite nanoclay particles. Previous work by the authors involved very limited morphological characterization of these materials using microscopy techniques,[15] which are further built upon here. Specifically, changes in the morphology of polyaniline are related to phase, conductivity, and adhesion force data collected on graphene oxide/polyaniline/Laponite (GOPL) nanocomposites with varying weight ratios of polyaniline:graphene oxide.

Experimental

Synthesis: GOPL composites were synthesized according to a previously published procedure.[15] Briefly, aniline polymerization was catalyzed by ammonium persulfate under acidic conditions in the presence of GO and Laponite. The GOPL80, GOPL50 and GOPL10 composites were synthesized respectively with 80:20:25, 50:50:25 and 10:90:25 weight ratios of GO:polyaniline:Laponite. The polyaniline is expected to exist predominantly in the conductive emeraldine oxidation state given the acidic synthetic conditions and the characteristic green color of the composites.[1] For each composite, 4 mg was dispersed in water with vigorous agitation and pipetted onto a glass slide, which were then allowed to very slowly air dry in a sealed, humid environment to yield GOPL films. Films prepared in this manner have a high bound water content important for proton-exchange mediated charge-transfer processes in polyaniline that lead to its high conductivity.[28] Note the use of Laponite here both as a synthetic templating reagent during polymerization and also as a film-forming agent. It was not possible to control film thickness using this casting method, but similar thicknesses of ~10 μm are expected on the basis of casting the same amount of material over the same substrate area.

Characterization: Scanning electron microscopy (SEM) data were collected using a Zeiss EVO W filament scanning electron microscope with a 9 kV emission potential. All AFM studies were carried out on an Asylum Research MFP-3D scanning probe microscope in ambient conditions. Topographical, phase and SMFS data were collected using Olympus AC160TS-R3 silicon probes with a tip radius of curvature of 9 ± 2 nm and spring constant of 11-54 N/m. For SMFS experiments, the spring constant of each cantilever was calibrated via the equipartition method, according to measurement of their thermal fluctuation.[29] Data were collected over 512 × 512 point grids covering 25 μm^2, 4 μm^2 and 1 μm^2 sample areas. Statistical characterization of the surfaces was carried out using the Gwyddion open-source software (version 2.53). Localized charge-transport properties were measured using Asylum ASYELEC-01 Ti-Ir coated silicon probes with a tip radius of curvature of 23 ± 10 nm and a spring constant of 0.5-4.4 N/m. For stable I-V response characterization, applied voltage biases ranged from 1 V up to 10 V.

Results and Discussion

The morphology of GOPL80, GOPL50 and GOPL10 were investigated via SEM, with representative micrographs presented in Figure 1. In GOPL80 there is clear preservation of the stacking of GO microsheets, upon which a small amount of globular polyaniline growth is visible (especially in the GO sheet in the centre of the micrograph). The visible globular polymer regions are on the order of about 50-1000 nm in size and display a large degree of spatial localization across the GO surface.

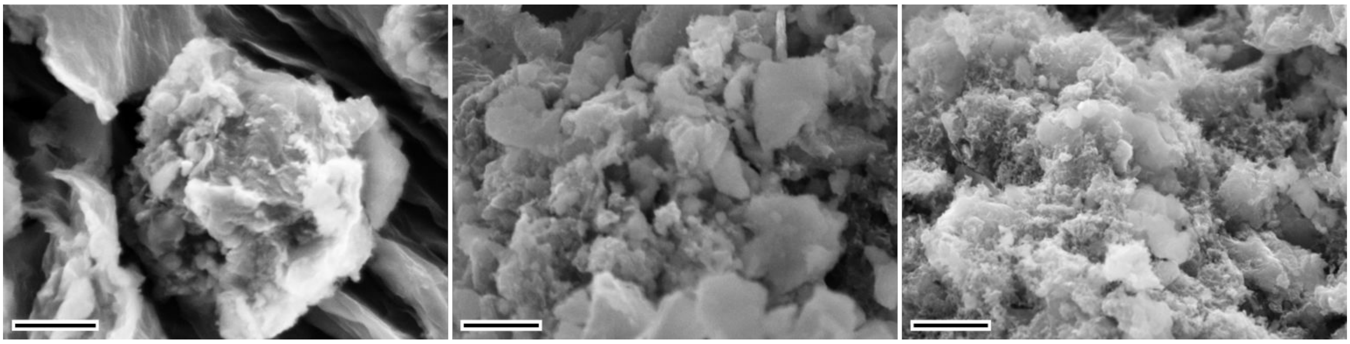

Figure 1. SEM images of (left to right) GOPL80, GOPL50 and GOPL10 with 2 μm scale bars.

The intermediate mass ratio of polyaniline in GOPL50 leads to increased globular growth which covers a larger fraction of the GO sheets. There is also a broader size distribution of globular structures, with polymer domains on the order of 50-2000 nm having good representation. While a few of the globular domains have grown quite large, they support and are surrounded by many smaller globular structures on the order of 50-500 nm. These smaller structures likely serve as a precursor morphology on which fibrous polyaniline can grow, although in general the connectivity between these domains is not extensive for this polymer loading.

At the highest polymer loading, GOPL10 contains extensive polyaniline growth over the GO microsheets. Globular polyaniline on the order of about 500-2000 nm in size is well represented throughout much of the micrograph. These domains are further surrounded by a dense web of fibrous polyaniline, extending in a large network across the micrograph. These nanofibers are 20-80 nm in diameter and typically extend for no more than 100 nm in length before connecting to other nanofibers or globular domains.

The GO sheets themselves seem to only directly support globular polymer growth, with fibrillar polyaniline then forming upon and between the globular domains. A templating action of the oxidized functional groups on GO sheets may be responsible for directing the growth of this polymer morphology. We have shown previously that polyaniline intercalates efficiently between GO sheets at high loadings, and that π-π and electrostatic interactions as well as charge-transfer processes are all important within the composite materials.[15] The fibrous polyaniline morphology that emerges with greater polymer loading has large surface area and high connectivity which are responsible for the large capacitance and good cycling stability of polyaniline and its composite materials.[30-31] A porous polymer network anchored to strong graphitic sheets also mitigates mechanical degradation that occurs due to swelling and shrinking of the polyaniline during solvent soaking and charge/discharge cycles.[32-34] Use in a solid-state device would eliminate the need for a solvent altogether, and further prolong functional lifetime.

The SEM micrographs provided here contain polyaniline which is similar in both size and morphology to previous reports.[15, 35-36] A better understanding of the differences between polyanilines of different micro- and nanostructure will allow optimization of synthetic procedures to produce structures best-suited to the desired application. To this end, AFM has been used to produce high-resolution spatial maps of polyaniline topography along with a better understanding of local mechanical and electrical properties within globular and fibrous polyaniline.

Topographical and phase maps of GOPL samples are shown in Figures 2 and 3 for 25 μm² and 1 μm² areas, respectively. The observed morphologies in the AFM data are consistent with the SEM data reported above, with evidence of boundaries between GO microsheets and increasing surface polymer growth at higher polyaniline loadings. The boundaries between GO terraces appear lighter yellow in the phase images. These stacking faults are likely key to the superior capacitive performance reported for similar nanocomposites,[1] as charges can be easily isolated between GO sheets. As the polymer loading was increased, darker overgrowths of fibrous polymer assemblies were observed in the tapping mode images. The darker polymer regions are most easily seen in Figure 3 in the phase images for GOPL50 (bottom right corner) and GOPL10 (throughout). These AFM images of GO/polyaniline heterointerfaces offer direct observation of the interfacial contacts which promote the charge-transfer interactions that are sought after in charge-storage devices.

The topographical data also provide measures of the surface roughness which contain important tribological information about the samples. Surface roughness is known to be of critical importance in nanoscale electrical devices, where in general it is preferable to have smoother surfaces at contact interfaces.[37] Table 1 shows the arithmetic average roughness (S_a), root-mean-squared roughness (S_q), and the ratio S_q/S_a for each sample.[38] The roughness values are larger in the larger film areas partly due to the microcrystalline structure of large graphene oxide sheets. Smaller film areas are generally smoother (lower roughness values) as structures local to individual graphene oxide sheet surfaces are observed. A Gaussian distribution of the surface roughness gives $S_q/S_a = 1.25$, and the experimental ratio is very close to this value in all cases for the composites studied here. On larger scales, the stacking efficiency of different graphene oxide sheets could be tuned by varying film drying time and Laponite clay loading to suit the desired application.

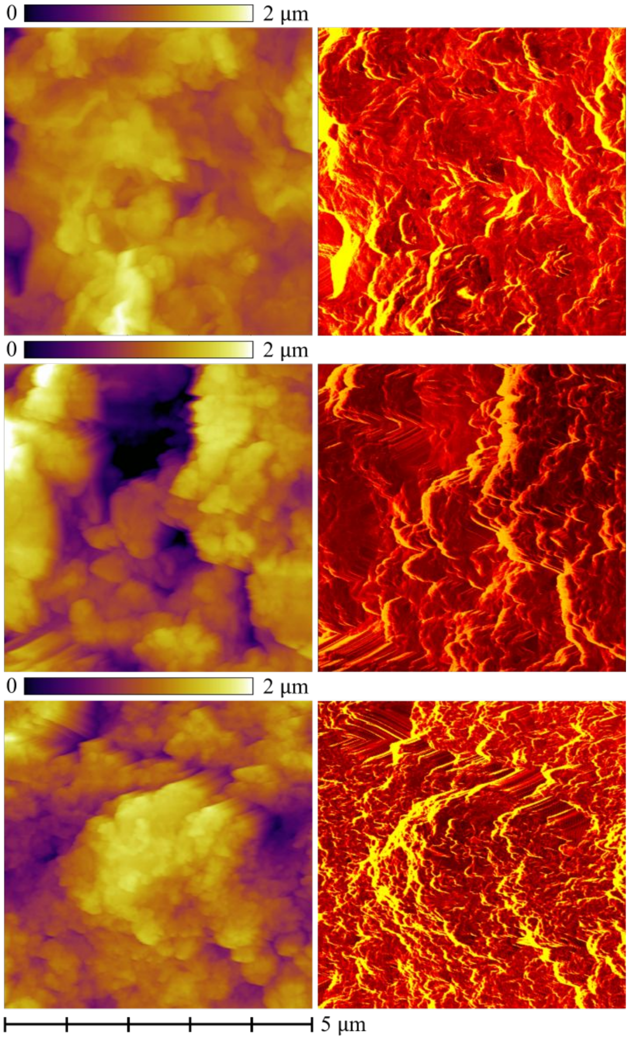

Figure 2. Topography (left) and phase (right) images for, top to bottom, GOPL80, GOPL50 and GOPL10 films collected over film areas of 25 μm^2.

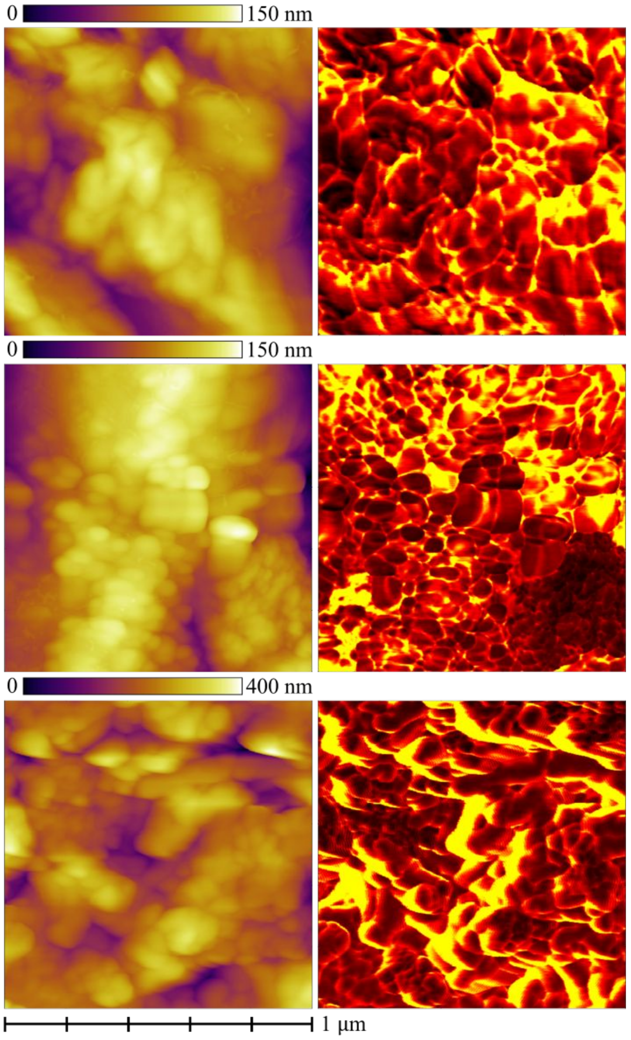

Figure 3. Topography (left) and phase (right) images for, top to bottom, GOPL80, GOPL50 and GOPL10 films collected over film areas of 1 μm^2.

Table 1. Surface roughness parameters for GOPL composite films over 25 μm^2 and 1 μm^2 film areas. Values are averages of 10-20 high quality topographical maps for each sample at each length scale.

Sample	Area (μm^2)	S_a (nm)	S_q (nm)	S_q/S_a
GOPL80	25	218 ± 65	276 ± 84	1.27
	1	49 ± 35	64 ± 48	1.30
GOPL50	25	205 ± 86	262 ± 109	1.28
	1	39 ± 14	50 ± 18	1.30
GOPL10	25	214 ± 101	273 ± 132	1.27
	1	86 ± 31	109 ± 37	1.26

Another way to characterize the surface properties is with the fractal dimension of the surface, which provides information about the self-affinity of topographical features in the sample. The fractal dimension D of the composite surfaces was obtained using the cube-counting method and the results are shown in Table 2. This fractal dimension D_{CC} increases as the polymer loading increases due to the statistical growth of polymer domains across the surfaces. For the relatively bare surface of the

GOPL80 composite, $D_{CC} = 2.14$ is quite close to the expected D = 2 for an ideally smooth surface. The Hurst exponent (or roughness parameter) H is given by $H = 3 - D$ and provides complementary information about the surface. Hurst exponents here range from 0.82-0.87, which are typical values for realistic rough surfaces.[39] Higher polymer loading leads to a rougher surface topography, and thus a larger Hurst exponent.

The power spectral density (PSD) provides further information about the surface roughness by characterizing the degree to which features of different spatial frequencies contribute to the surface structure. A thorough description of surface topography characterization using spectral analysis exists elsewhere.[40] For a 2D micrograph the PSD is a 2D image in frequency space, and is obtained by taking the Fourier transform of the height autocorrelation function:

$$PSD(k_x,k_y) = \left(\frac{1}{L}\right)^2 \left| \int_0^L dx\, e^{-ik_x x} \int_0^L dy\, e^{-ik_y y} h(x,y) \right|^2$$

where L is the scan size (i.e. the side length of an AFM image), $h(x,y)$ is the measured height profile, and k_x and k_y are spatial frequencies in the short and long scan directions respectively. For isotropic surfaces the PSD is independent of the azimuthal angle, and the radial PSD can be described by a single spatial frequency $k = \sqrt{k_x + k_y}$. Since the AFM data are non-periodic, Hann windowing is applied before the PSD calculation to prevent the introduction of artifacts caused by the edges of the image. The PSD data is bounded by the short and long wavelength cutoffs: for an image of side length L containing N pixels per row, k is uniformly spaced along ${}^{2\pi}/_{L}$ to ${}^{N\pi}/_{L}$ in frequency space.

The 2D and corresponding radial PSD for GOPL10 are shown in Figure 4, with good overlap between the PSD functions calculated at the 5 μm and 1 μm length scales. Surface analysis using the radial PSD is justified by the clear radial symmetry in the 2D PSD. The data for GOPL50 and GOPL80 have a very similar appearance. The isotropic PSD shows that there is no preferred orientation of the surface features, and that surface polymerization occurs without a preferred growth direction on GO sheets. For charge storage applications an isotropic polymer growth mechanism helps prevent charge leakage and thus improves charge storage duration. If charge transport rather than charge storage is the desired polymer functionality then a synthetic scheme that produces anisotropic polymer growth is preferable.[41]

Surfaces which possess self-affinity across multiple scales will have a power law decay $PSD(k) = wk^{-\alpha}$ for constant w and critical exponent α. The critical exponent is related to the Hurst exponent by $\alpha = 2(1 + H)$. The PSD data are fit well over several decades by $\alpha \approx 3.8$, indicating self-affinity over these length scales. This value of α corresponds to H ≈ 0.9 which is similar to the value obtained from fractal dimensional analysis. The lack of a significant roll-off (i.e. $PSD(k) \approx$ const.) at low spatial frequencies (large features) indicates that self-affinity extends to features greater than the AFM scan sizes. The relative self-affine scaling constants w^{rel} for the different composite samples (Table 2) follow a qualitatively similar trend to the S_q roughness values.

For higher spatial frequencies the resolution of surface features eventually becomes limited by the probe radius. For the ~10 nm tip used in this experiment spatial frequencies approaching 10^8 m^{-1} become prone to artifacts, and the ability to accurately measure feature with $k > 10^8$ m^{-1} is diminished.

Table 2. Statistical parameters of the composite surfaces: fractal dimension D_{CC} from cube-counting, corresponding Hurst exponent, and the self-affine scaling constant w.

Composite	D_{CC}	H	w^{rel}
GOPL80	2.13 ± 0.04	0.87 ± 0.04	1.0

GOPL50	2.14 ± 0.02	0.86 ± 0.02	0.3
GOPL10	2.18 ± 0.03	0.82 ± 0.03	1.7

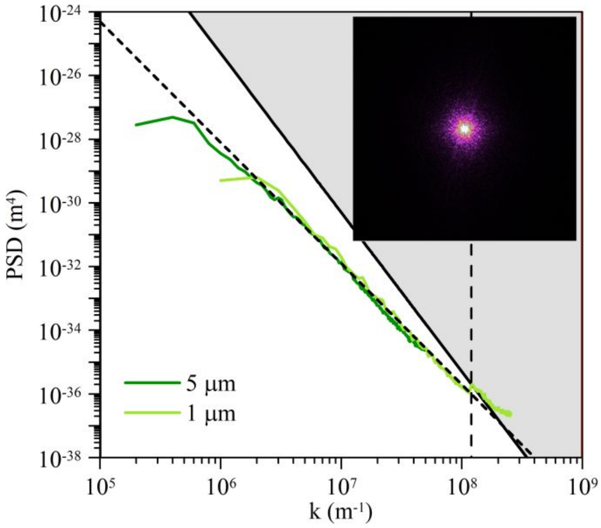

Figure 4. Radial power spectral density of the GOPL10 composite surface. Inset is the 2D PSD with Hann windowing. The dashed black line extending through the data is a power law fit, the vertical dashed line corresponds to feature sizes equal to the tip radius, and the area near and above the solid black line ($PSD(k) \propto k^{-5}$) that is shaded grey is unreliable for the ~10 nm tip used.[40]

The distribution of adhesion forces between the AFM tip and the sample surfaces are shown in Figure 5. These distributions are characterized in Table 3 by the most frequently occurring interaction force (F_{peak}), the arithmetic mean interaction force ($\langle F \rangle$), and the maximum (strongest) interaction force (F_{max}).

The adhesion force distribution for GOPL80 peaks sharply at 15 nN, and there are very few interactions involving forces greater than 100 nN for this composite. The distribution extends up to F_{max} at 300 nN, with $\langle F \rangle$ of 30 nN. This high GO fraction composite exhibits predominantly weak interactions with the AFM tip, with a narrow distribution of adhesion forces as previously observed.[42]

In GOPL50 the adhesion force distribution also peaks sharply at low interaction force of ~20 nN, with a shoulder at ~50 nN representing increased frequency of stronger interactions. There are also a significant number of interactions occurring in the 100-300 nN range for this composite, decreasing in incidence up to F_{max} at 500 nN. The higher incidence of these larger force interactions increases $\langle F \rangle$ to 60 nN. It is expected that the increase in polymer growth size and improved coverage in the intermediate composite is producing these stronger adhesive interactions with the AFM tip, especially considering the greater interfacial contact produced when the tip is depressed into fibrous polyaniline which starts to become visible with this polymer loading.

The adhesion force distribution of GOPL10 peaks much higher at 60 nN. There is also a very large fraction of interactions involving much greater forces, which extend to F_{max} at 1600 nN. This much broader distribution leads to an appreciably higher $\langle F \rangle$ value of 200 nN. In addition, weak interactions with GO that produced interaction forces below 50 nN were commonplace in GOPL80 and GOPL50, but are almost completely absent in this sample. This is attributed to large interfacial contact between the tip with the dense fibrous polymer domains shown in the SEM and AFM micrographs, which completely cover the GO sheets at this high polymer loading.

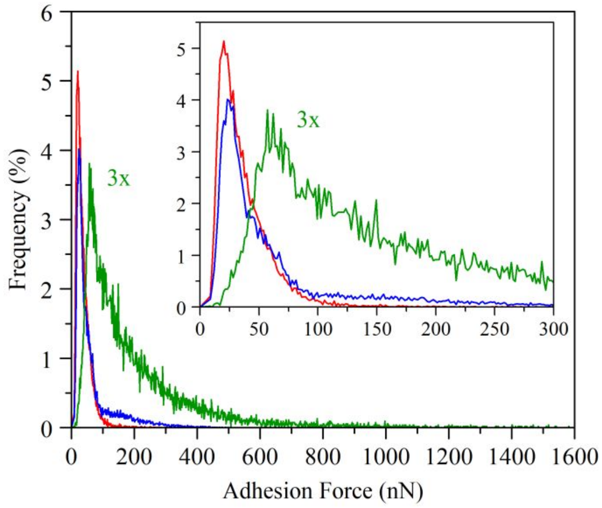

Figure 5. Adhesion force distributions between the AFM tip and GOPL80 (—), GOPL50 (—) and GOPL10 (—) surfaces. Inset is a magnification of the 0-300 nN force range. Frequency is expressed as a percent of the total number of individual extension-retraction force curves that comprise surface maps of the tip-sample adhesion forces. The distribution for GOPL10 is scaled by a factor of 3 for clarity.

Table 3. Characteristics of the adhesion force distributions in Figure 5.

Composite	F_{peak} (nN)	$\langle F \rangle$ (nN)	F_{max} (nN)
GOPL80	15	30	300
GOPL50	20	60	500
GOPL10	60	200	1600

Finally, we investigate how different polymer loadings affects the electrical properties of the composite surfaces. Figure 6 shows conductive AFM data for the GOPL nanocomposite films at varied polyaniline loadings. Conductive polyaniline domains are evident in the lighter regions of the cAFM maps. Despite long collection times, indistinguishable topographical and current maps collected from several repeated cAFM scans over the same film areas suggest good mechanical and electrochemical stability of the composites during redox cycling. We note here very generally that inclusion of Laponite nanoparticles led to significantly improved film quality while still maintaining polyaniline conductivity, for which some evidence had previously been demonstrated.[15] We have recently reported similar improvements in polydispersity and conductive performance in Laponite/carbon nanotube films.[43]

In GOPL80 the lack of evidence for significant polymer growth in the topography and phase maps is consistent with the absence of regions of high conductivity in the conductivity map. The current for this sample is extremely small, on the order of only ~10 pA. Previous work has shown similarly negligible I-V current responses for graphene oxide surfaces.[23] Despite this, there are some regions of elevated conductivity up to 32 pA on the surface which may be caused by the presence of small amounts of polyaniline. This is consistent with the data for GOPL50 where increased polymer growth leads to a proliferation of higher conductivity regions, and the current in the conductive regions increases up to 52 pA. Although it was not possible to control the thickness of the composite films, the film casting procedure gives all films a nominal thickness of ~10 μm. Despite variations in surface height above the substrate, very similar results were observed for 5-15 other high-quality current maps taken at different locations on these composite films.

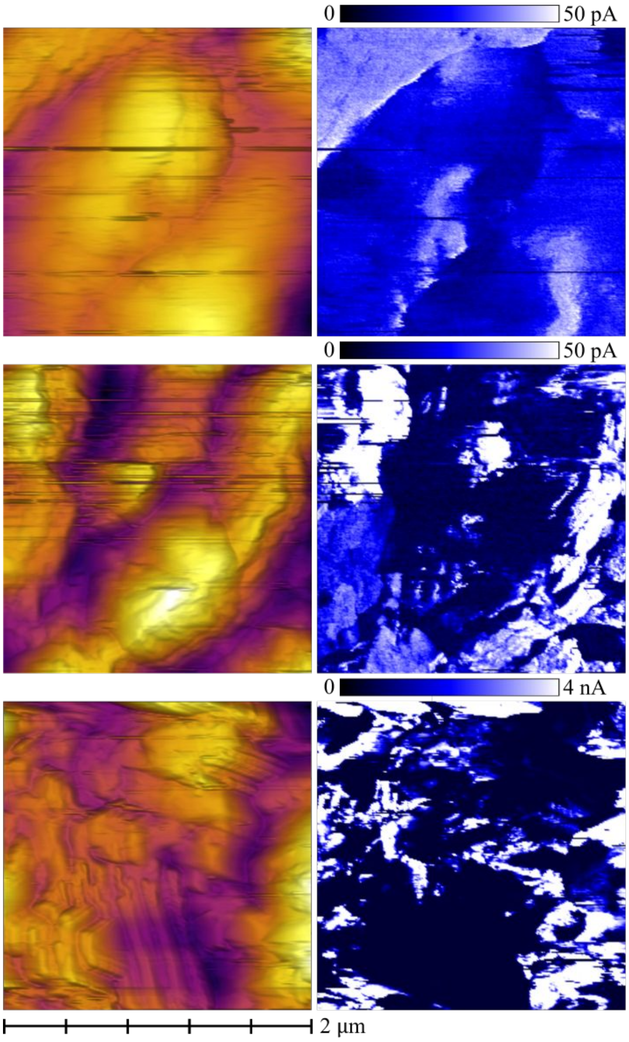

Figure 6. Topography (left) and current (right) images for, top to bottom, GOPL80, GOPL50 and GOPL10 films collected over film areas of 4 µm^2. Note that in order to display the data for GOPL10, the colour scale is changed from 0-50 pA for GOPL80 and GOPL50 to 0-4 nA for GOPL10.

The data for GOPL10 is very different than for the other two samples, and demonstrates currents as high as 6.1 nA in some regions. Currents of this magnitude are consistent with previous work on pure polyaniline films.[22] The current map for GOPL10 shown in Figure 6 contains some regions that are dominated by polymer growth and others that expose bare graphene oxide. For example, in the bottom right of the current map there are bright regions with currents of ~3 nA, while directly adjacent to these is a region of negligible current that presents as a stacked graphitic architecture in the topography map. The I-V response for this sample is likely appreciably larger due to the increased polyaniline composition, and the resulting fibrous network that penetrates extensively through the sample as shown in Figures 1-3. This high polymer connectivity was not observed throughout much of the GOPL80 and GOPL50 samples, where low polyaniline loading lead to predominantly globular and spatially localized polymer growth. The sparsity and poor connectivity of the polymer domains in these samples likely explains the very low I-V response of these samples to the applied bias.

Conclusions

Water based self-assembly strategies combined with *in situ* polymerization of aniline in colloidal dispersions of graphene oxide and Laponite nanoparticles afforded nanocomposites of polyaniline included within graphene oxide nanosheets. The inclusion of the Laponite nanoparticles led to improved aqueous phase polydispersity and superior film formation. Using the combined suite of AFM techniques reported here we were able to track changes in the morphology, mechanical, and electrical properties of the polymer composites as a function of the polymer weight loading. Studies of this nature will hopefully be used to relate the quality of device performance to the material architectures and heterointerfacial interactions, and to enable the rational design of materials for a given application.

Acknowledgments

The authors would like to thank the National Science Foundation (CMMI-1342577, DMR-1229142, and EEC-0939322). We thank Mark Hooker, Rebecca Cortez, Don Dobbs, and Yifei Zhu for materials and characterization support.

References

1. Zhang, K.; Zhang, L. L.; Zhao, X. S.; Wu, J. S., Graphene/Polyaniline Nanofiber Composites as Supercapacitor Electrodes. *Chem Mater* **2010,** *22* (4), 1392-1401.
2. Salvatierra, R. V.; Cava, C. E.; Roman, L. S.; Zarbin, A. J. G., ITO-Free and Flexible Organic Photovoltaic Device Based on High Transparent and Conductive Polyaniline/Carbon Nanotube Thin Films. *Adv Funct Mater* **2013,** *23* (12), 1490-1499.
3. Du, Y.; Shen, S. Z.; Yang, W. D.; Donelson, R.; Cai, K. F.; Casey, P. S., Simultaneous increase in conductivity and Seebeck coefficient in a polyaniline/graphene nanosheets thermoelectric nanocomposite. *Synthetic Met* **2012,** *161* (23-24), 2688-2692.
4. Al-Mashat, L.; Shin, K.; Kalantar-Zadeh, K.; Plessis, J. D.; Han, S. H.; Kojima, R. W.; Kaner, R. B.; Li, D.; Gou, X. L.; Ippolito, S. J.; Wlodarski, W., Graphene/Polyaniline Nanocomposite for Hydrogen Sensing. *J Phys Chem C* **2010,** *114* (39), 16168-16173.
5. Sun, Y. B.; Shao, D. D.; Chen, C. L.; Yang, S. B.; Wang, X. K., Highly Efficient Enrichment of Radionuclides on Graphene Oxide-Supported Polyaniline. *Environ Sci Technol* **2013,** *47* (17), 9904-9910.
6. Tran, H. D.; D'Arcy, J. M.; Wang, Y.; Beltramo, P. J.; Strong, V. A.; Kaner, R. B., The oxidation of aniline to produce "polyaniline": a process yielding many different nanoscale structures. *J Mater Chem* **2011,** *21* (11), 3534-3550.
7. Bon, S. A. F.; Colver, P. J., Pickering miniemulsion polymerization using Laponite clay as a stabilizer. *Langmuir* **2007,** *23* (16), 8316-8322.
8. Kehlbeck, J. D.; Hagerman, M. E.; Cohen, B. D.; Eliseo, J.; Fox, M.; Hoek, W.; Karlin, D.; Leibner, E.; Nagle, E.; Nolan, M.; Schaefer, I.; Toney, A.; Topka, M.; Uluski, R.; Wood, C., Directed self-assembly in laponite/CdSe/polyaniline nanocomposites. *Langmuir* **2008,** *24* (17), 9727-9738.
9. Ruzicka, B.; Zulian, L.; Angelini, R.; Sztucki, M.; Moussaid, A.; Ruocco, G., Arrested state of clay-water suspensions: Gel or glass? *Phys Rev E* **2008,** *77* (2).
10. Ruzicka, B.; Zaccarelli, E., A fresh look at the Laponite phase diagram. *Soft Matter* **2011,** *7* (4), 1268-1286.
11. Avery, R. G.; Ramsay, J. D. F., Colloidal Properties of Synthetic Hectorite Clay Dispersions .2. Light and Small-Angle Neutron-Scattering. *J Colloid Interf Sci* **1986,** *109* (2), 448-454.
12. Alhassan, S. M.; Qutubuddin, S.; Schiraldi, D. A., Graphene Arrested in Laponite-Water Colloidal Glass. *Langmuir* **2012,** *28* (8), 4009-4015.
13. Yoo, J.; Lee, S. B.; Lee, C. K.; Hwang, S. W.; Kim, C.; Fujigaya, T.; Nakashima, N.; Shim, J. K., Graphene oxide and laponite composite films with high oxygen-barrier properties. *Nanoscale* **2014,** *6* (18), 10824-10830.
14. Li, X. W.; Zhou, M.; Xu, H. L.; Wang, G. C.; Wang, Z., Synthesis and electrochemical performances of a novel two-dimensional nanocomposite: polyaniline-coated laponite nanosheets. *J Mater Sci* **2014,** *49* (19), 6830-6837.

15. Ramphal, I. A.; Hagerman, M. E., Water-Processable Laponite/Polyaniline/Graphene Oxide Nanocomposites for Energy Applications. *Langmuir* **2015,** *31* (4), 1505-1515.

16. Garcia, R.; Gomez, C. J.; Martinez, N. F.; Patil, S.; Dietz, C.; Magerle, R., Identification of nanoscale dissipation processes by dynamic atomic force microscopy. *Phys Rev Lett* **2006,** *97* (1).

17. Kim, Y.; Kim, W.; Park, J. W., Principles and Applications of Force Spectroscopy Using Atomic Force Microscopy. *B Korean Chem Soc* **2016,** *37* (12), 1895-1907.

18. Wang, D.; Russell, T. P., Advances in Atomic Force Microscopy for Probing Polymer Structure and Properties. *Macromolecules* **2018,** *51* (1), 3-24.

19. Dewolf, P.; Snauwaert, J.; Clarysse, T.; Vandervorst, W.; Hellemans, L., Characterization of a Point-Contact on Silicon Using Force Microscopy-Supported Resistance Measurements. *Appl Phys Lett* **1995,** *66* (12), 1530-1532.

20. Khalid, M.; Tumelero, M. A.; Zoldan, V. C.; Cid, C. C. P.; Franceschini, D. F.; Timm, R. A.; Kubota, L. T.; Moshkalev, S. A.; Pasa, A. A., Polyaniline nanofibers-graphene oxide nanoplatelets composite thin film electrodes for electrochemical capacitors. *Rsc Adv* **2014,** *4* (64), 34168-34178.

21. Wei, D.; Li, H. W.; Han, D. X.; Zhang, Q. X.; Niu, L.; Yang, H. F.; Bower, C.; Andrew, P.; Ryhanen, T., Properties of graphene inks stabilized by different functional groups. *Nanotechnology* **2011,** *22* (24).

22. Wu, C. G.; Chang, S. S., Nanoscale measurements of conducting domains and current - Voltage characteristics of chemically deposited polyaniline films. *J Phys Chem B* **2005,** *109* (2), 825-832.

23. Ekiz, O. O.; Urel, M.; Guner, H.; Mizrak, A. K.; Dana, A., Reversible Electrical Reduction and Oxidation of Graphene Oxide. *Acs Nano* **2011,** *5* (4), 2475-2482.

24. Suk, J. W.; Piner, R. D.; An, J. H.; Ruoff, R. S., Mechanical Properties of Mono layer Graphene Oxide. *Acs Nano* **2010,** *4* (11), 6557-6564.

25. Froning, J. P.; Lazar, P.; Pykal, M.; Li, Q.; Dong, M. D.; Zboril, R.; Otyepka, M., Direct mapping of chemical oxidation of individual graphene sheets through dynamic force measurements at the nanoscale. *Nanoscale* **2017,** *9* (1), 119-127.

26. Passeri, D.; Tamburri, E.; Terranova, M. L.; Rossi, M., Polyaniline-nanodiamond fibers resulting from the self-assembly of nano-fibrils: a nanomechanical study. *Nanoscale* **2015,** *7* (34), 14358-14367.

27. Jafarzadeh, S.; Claesson, P. M.; Sundell, P. E.; Pan, J. S.; Thormann, E., Nanoscale Electrical and Mechanical Characteristics of Conductive Polyaniline Network in Polymer Composite Films. *Acs Appl Mater Inter* **2014,** *6* (21), 19168-19175.

28. Travers, J. P.; Nechtschein, M., Water Effects in Polyaniline - a New Conduction Process. *Synthetic Met* **1987,** *21* (2), 135-141.

29. Butt, H. J.; Jaschke, M., Calculation of Thermal Noise in Atomic-Force Microscopy. *Nanotechnology* **1995,** *6* (1), 1-7.

30. Chen, H.; Chen, J. S.; Zhou, H. H.; Jiao, S. Q.; Chen, J. H.; Kuang, Y. F., The application of nano-fibrous polyaniline in electrochemical capacitor. *Acta Phys-Chim Sin* **2004,** *20* (6), 593-597.

31. Ansari, S. A.; Parveen, N.; Han, T. H.; Ansari, M. O.; Cho, M. H., Fibrous polyaniline@manganese oxide nanocomposites as supercapacitor electrode materials and cathode catalysts for improved power production in microbial fuel cells. *Phys Chem Chem Phys* **2016,** *18* (13), 9053-9060.

32. Luo, J. W.; Zhong, W. B.; Zou, Y. B.; Xiong, C. L.; Yang, W. T., Preparation of morphology-controllable polyaniline and polyaniline/graphene hydrogels for high performance binder-free supercapacitor electrodes. *J Power Sources* **2016,** *319*, 73-81.

33. Wu, Q.; Xu, Y. X.; Yao, Z. Y.; Liu, A. R.; Shi, G. Q., Supercapacitors Based on Flexible Graphene/Polyaniline Nanofiber Composite Films. *Acs Nano* **2010,** *4* (4), 1963-1970.

34. Wang, H. L.; Hao, Q. L.; Yang, X. J.; Lu, L. D.; Wang, X., Effect of Graphene Oxide on the Properties of Its Composite with Polyaniline. *Acs Appl Mater Inter* **2010,** *2* (3), 821-828.

35. Mondschein, J. S.; Kowalski, A.; Kehlbeck, J. D.; Hagerman, M. E.; Cortez, R., Comparative AFM studies of water processable polyaniline films: Influence of reaction time on nanomorphology and conductivity. *Mater Lett* **2014,** *131*, 262-265.

36. Avlyanov, J. K.; Josefowicz, J. Y.; Macdiarmid, A. G., Atomic-Force Microscopy Surface-Morphology Studies of in-Situ Deposited Polyaniline Thin-Films. *Synthetic Met* **1995,** *73* (3), 205-208.

37. Sohn, M. H.; Kim, D.; Kim, S. J.; Paik, N. W.; Gupta, S., Super-smooth indium-tin oxide thin films by negative sputter ion beam technology. *J Vac Sci Technol A* **2003,** *21* (4), 1347-1350.

38. Gadelmawla, E. S.; Koura, M. M.; Maksoud, T. M. A.; Elewa, I. M.; Soliman, H. H., Roughness parameters. *J Mater Process Tech* **2002,** *123* (1), 133-145.

39. Persson, B. N. J., On the Fractal Dimension of Rough Surfaces. *Tribol Lett* **2014,** *54* (1), 99-106.

40. Jacobs, T. D. B.; Junge, T.; Pastewka, L., Quantitative characterization of surface topography using spectral analysis. *Surf Topogr-Metrol* **2017,** *5* (1).

41. Chidembo, A. T.; Aboutalebi, S. H.; Konstantinov, K.; Wexler, D.; Liu, H. K.; Dou, S. X., Liquid Crystalline Dispersions of Graphene-Oxide-Based Hybrids: A Practical Approach towards the Next Generation of 3D Isotropic Architectures for Energy Storage Applications. *Part Part Syst Char* **2014,** *31* (4), 465-473.

42. Ding, Y. H.; Zhang, P.; Ren, H. M.; Zhuo, Q.; Yang, Z. M.; Jiang, X.; Jiang, Y., Surface adhesion properties of graphene and graphene oxide studied by colloid-probe atomic force microscopy. *Appl Surf Sci* **2011,** *258* (3), 1077-1081.

43. Valdman, L.; Dobbs, D.; Cortez, R.; Hagerman, M. E., Improving conductivity in carbon nanotube percolating networks through inclusion of Laponite nanoparticles. *Mater Lett* **2018,** *217*, 88-91.

For Table of Contents Only: